ACS APPLIED NANO MATERIALS
Article
Cite This: ACS Appl. Nano Mater. 2018, 1, 3969−3980
www.acsanm.org

High Aspect Ratio Carboxycellulose Nanofibers Prepared by Nitro-Oxidation Method and Their Nanopaper Properties

Priyanka R. Sharma, Bingqian Zheng, Sunil K. Sharma, Chengbo Zhan, Ruifu Wang, Surita R. Bhatia, and Benjamin S. Hsiao*

Department of Chemistry, Stony Brook University, Stony Brook, New York 11794-3400, United States

Supporting Information

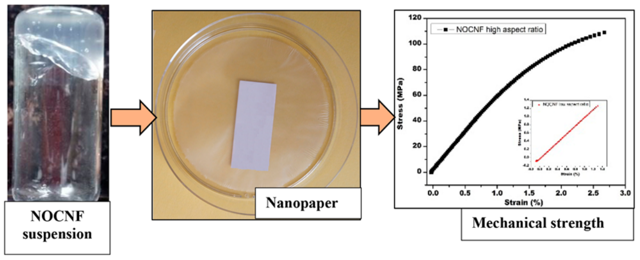

ABSTRACT: High aspect ratio carboxycellulose nanofibers (NOCNF), having typical length over 1000 nm, width ∼4.6 nm, thickness ∼1.3 nm, and carboxylate content of 0.42 mmol/g, were extracted from jute fibers using a modified nitro-oxidation method. The extracted nanofiber was found to possess crystallinity of 69% (measured by wide-angle X-ray diffraction, WAXD), relatively higher than that of raw jute fibers (crystallinity ∼61%). Gelation of NOCNF in aqueous suspensions was observed due to the high aspect ratio of the fiber even at a relatively low concentration. Rheological studies on the NOCNF suspensions at different concentrations (0.01−1 wt %) revealed the shear-thinning behavior with increasing shear rate. The corresponding viscoelastic moduli (G' and G'') results indicated that the NOCNF suspension at concentration between 0.1 and 0.2 wt % possessed a liquid−gel transition. The rheological data near the gelation point could be fitted by the Winter−Chambon model, where the results confirmed the formation of a percolated fibrous network. The flow behavior of the NOCNF suspensions in the chosen concentration range could be further described by the concept of the crowding factor. Nanopaper prepared using these high aspect ratio carboxycellulose nanofibers exhibited good mechanical properties with tensile strength of 108 ± 2 MPa and Young's modulus of 4.1 ± 0.2 GPa.

KEYWORDS: *carboxycellulose, nanofibers, nitro-oxidation, rheology, gelation, crowding factor, nanopaper*

■ INTRODUCTION

Due to high sustainability, renewability, and low cost, cellulose is a reliable source for materials development in a wide range of applications, from traditional packaging materials to fuels and chemicals. In the past two decades, the development of functional nanoscale cellulose has enabled the usage of nanocellulose in many advanced applications, such as biomedical devices,[1,2] solar cells,[3,4] fuel cells,[5] fluorescent bioimaging molecules,[6] drug delivery,[7] gas barrier films,[5,8] water purification,[9,10] sensors,[11] dispersion stabilizer of carbon nanotubes in aqueous phase,[12] flexible electronics,[13−15] electrocatalyst,[16] etc. There are different kinds of nanoscale celluloses, including cellulose nanocrystals (CNC),[17−19] cellulose nanofibers (CNF),[20,21] microfibrillated cellulose (MFC),[22] and spherical nanocellulose.[7,23,24] Recently, TAPPI has announced the criteria to define the appropriate nomenclature of nanostructured cellulose.[19] In these nanomaterials, CNC is usually extracted by the acid hydrolysis method, while CNF and MFC are produced by chemical and mechanical treatments. It has also been reported that the introduction of surface charges on cellulose can facilitate the fibrillation of CNF due to the electrical repulsion forces between the charged nanofibers.[20]

Typical industrial processes to produce nanocellulose include acid hydrolysis,[17,25,26] carboxylation,[27−29] carboxymethylations,[30] and quaternization,[31] followed by mechanical treatment such as high pressure homogenization and ultrasonication. Most of these methods require the use of only cellulose as a source to extract nanocellulose.[18,32,33] Recently, our laboratory has demonstrated a simple nitro-oxidation method that can extract carboxycellulose nanofibers (NOCNF) directly from untreated biomass (containing cellulose, hemicellulose, and lignin), such as raw jute and spinifex fibers, using the mixture of nitric acid and sodium nitrite.[29] Although the use of nitro-oxidation method to prepare carboxycellulose microfibers has been demonstrated earlier,[12] the discovery of its usage to extract carboxycellulose nanofibers from biomass was only recent.[34] It was further observed that NOCNF could be an excellent adsorbent/coagulant for removal of heavy metal ions from water.[32] However, the NOCNF produced in our earlier study[25] was of low aspect ratio (length = 190−370 nm; diameter = 4−5 nm), limiting their applications as structural materials (e.g., for fabrication of membranes and nanocomposites). The purpose of this study was to optimize the nitro-oxidation method that could produce high aspect ratio NOCNF to exhibit gel behavior and to enhance mechanical properties when fabricated into the form of nanopaper.

Received: May 4, 2018
Accepted: July 17, 2018
Published: July 17, 2018

DOI: 10.1021/acsanm.8b00744
ACS Appl. Nano Mater. 2018, 1, 3969−3980

The hypothesis behind the nitro-oxidation method, using the mixture of nitric acid and sodium nitrite, to treat dry biomass, involves the simultaneous pretreatment and oxidation of biomass, leading to nanofibrillation of the cellulose component. Specifically, the presence of nitrogen oxide species (produced by the addition of nitric acid and sodium nitrite) can depolymerize the lignin component by converting the syringyl units on lignin into soluble benzoquinone products.[35] In addition, the hemicellulose component can be broken down into xylose and other byproducts by nitric acid.[36] Furthermore, the generation of nitrosonium ions (an active oxidizing species) through the reaction of nitric acid and sodium nitrite can selectively oxidize the primary hydroxyl groups of anhydroglucose units of cellulose to carboxyl groups. The schematic of oxidation of cellulose by nitrosonium ion has been described in our earlier study.[29]

In this study, we have fine-tuned the reaction conditions in the nitro-oxidation treatment of raw jute fibers to produce high aspect ratio NOCNF, which exhibited a distinct liquid−gel transition in the suspension state. In the literature, high aspect ratio nanocellulose could be prepared by varying processes, including TEMPO-oxidation, carboxymethylation, homogenization, and microfluidization[37−39] to prepare membrane materials with good mechanical strength, decent thixotropic properties, and high thermal stability. The reaction conditions of the nitro-oxidation method in the current study have been carefully optimized to produce NOCNF with properties comparable with those prepared by other methods. Specifically, the structure—property (thermal, rheological, and mechanical)—processing relationships in the fabrication of NOCNF are discussed. Furthermore, the rheological properties of the NOCNF suspension near the liquid−gel transition were described by the Winter−Chambon model as well as by the concept of the crowding factor. Finally, we demonstrate the preparation of NOCNF-based nanopaper with very good mechanical properties, compared with those prepared by other methods.

■ EXPERIMENTAL SECTION

Materials. Dried jute fibers (degree of polymerization (DP) of the extracted cellulose was 516) were provided by Toptrans Bangladesh Ltd. in Dhaka, Bangladesh. Untreated fibers were first cut into small pieces, having 3−5 cm in length, and subsequently washed without further treatment. Analytical grade nitric acid (ACS reagent, 60%) and sodium nitrite (ACS reagent, ≥97%) were purchased from Sigma-Aldrich; sodium bicarbonate was purchased from Fisher Scientific. All chemicals were used without further purification.

Preparation of NOCNF from Jute Fibers. Finely cut jute fibers were dipped in sodium hydroxide (1N) solution for 24 h at room temperature. These fibers were subsequently washed using distilled water, treated with microfiltration until the filtrate became neutral (pH = 7), and collected and dried in an oven at 60 °C for 14 h. These dried jute fiber samples were then utilized to extract NOCNF using the previously published nitro-oxidation method[29] with modified reaction conditions using a lower concentration nitric acid. Specifically, 10 g of finely cut dried jute fibers was placed in a 1 L three-neck round-bottom flask, where 14 mL (22.2 mmol) of nitric acid (60%) was subsequently added. When the samples became completely soaked in the acid, 0.96 g of sodium nitrite (14 mmol) was added to the reaction mixture under continuous stirring. Upon the addition of sodium nitrite, red fumes were formed inside the flask. To prevent the red fumes from escaping, the mouths of the round-bottom flask were closed with stoppers. The reaction was performed at 50 °C for 12 h and was then quenched by adding 250 mL of distilled water to the beaker. Once the final product was equilibrated, the supernatant liquid was discarded to remove the excess acid, leaving behind the solid product. After performing the first decantation process, a mixture of ethanol and water (1:2 ratio) was added to the solid product, and then the suspension was stirred using a glass rod. The sample was untouched until the liquid (supernatant) and solid became separate layers. The supernatant was also decanted off to extract the solid product. The above decantation step was repeated 4−5 times, until the pH value of the suspension reached above 2.5. This suspension was then transferred into a dialysis bag (Spectral/Por; molecular weight cut-off, MWCO: 6−8 kDa) and equilibrated for 4−5 days until the conductivity of water reached below 5 μS. The resulting cellulose product possessed the carboxyl (COOH) group. To obtain a good dispersion of nanofibers with ionic properties (COO^-Na^+), the functionalized nanocellulose was then treated with 8 wt % sodium bicarbonates (1:10 w/v), until the pH of suspension reached 7.5. The sample was again dialyzed (using a dialysis bag, Spectral/Por; with MWCO: 6−8 kDa) and equilibrated for 2−4 days, until the conductivity of water reached below 5 μS. The sample slurry (0.2 wt %) was then homogenized using a high pressure homogenizer (GEA Niro Soavi Panda Plus Bench top homogenizer), at 250 bar for 1 cycle. The schematic diagram on preparation of NOCNF using the nitro-oxidation approach is shown in Figure 1.

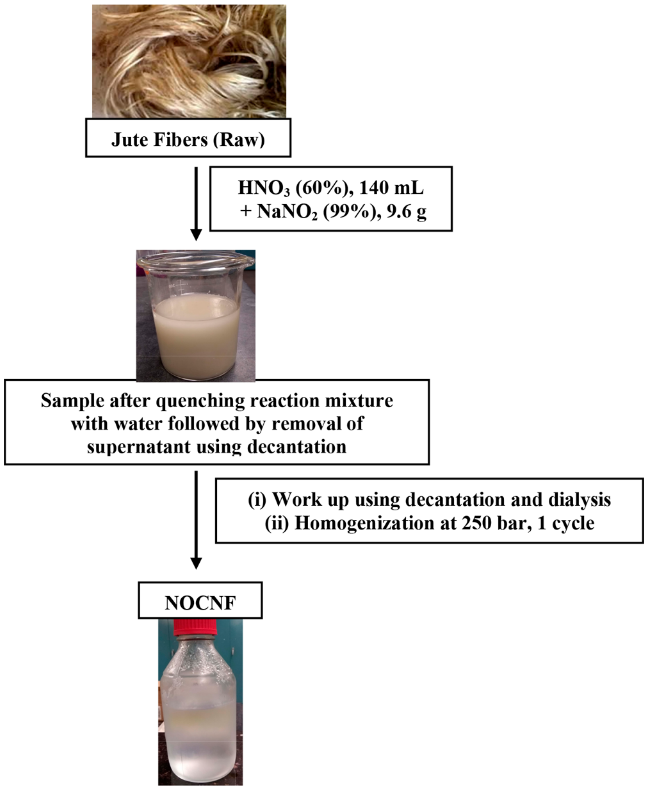

Figure 1. Schematic diagram on preparation of NOCNF using the nitro-oxidation method.

Characterization of NOCNF. The carboxylate content and aldehyde content of NOCNF were determined using the conductometric titration method. The detailed description of the titration procedure is discussed in the Supporting Information. Furthermore, the surface charge of NOCNF was determined by measuring the ζ-potential of the suspension (using Zetaprobe Analyzer—Colloid Dynamics). The structural and functional characterizations of NOCNF were carried out using Fourier transform infrared spectrometer (FTIR, PerkinElmer Spectrum One instrument using the attenuated total reflectance (ATR) mode), ^{13}C CPMAS nuclear magnetic resonance (NMR, Bruker Utrashield 500WB plus 500 MHz NMR instrument), wide-angle X-ray diffraction (WAXD, Benchtop Rigaku MiniFlex 600), and thermogravimetric analysis (PerkinElmer

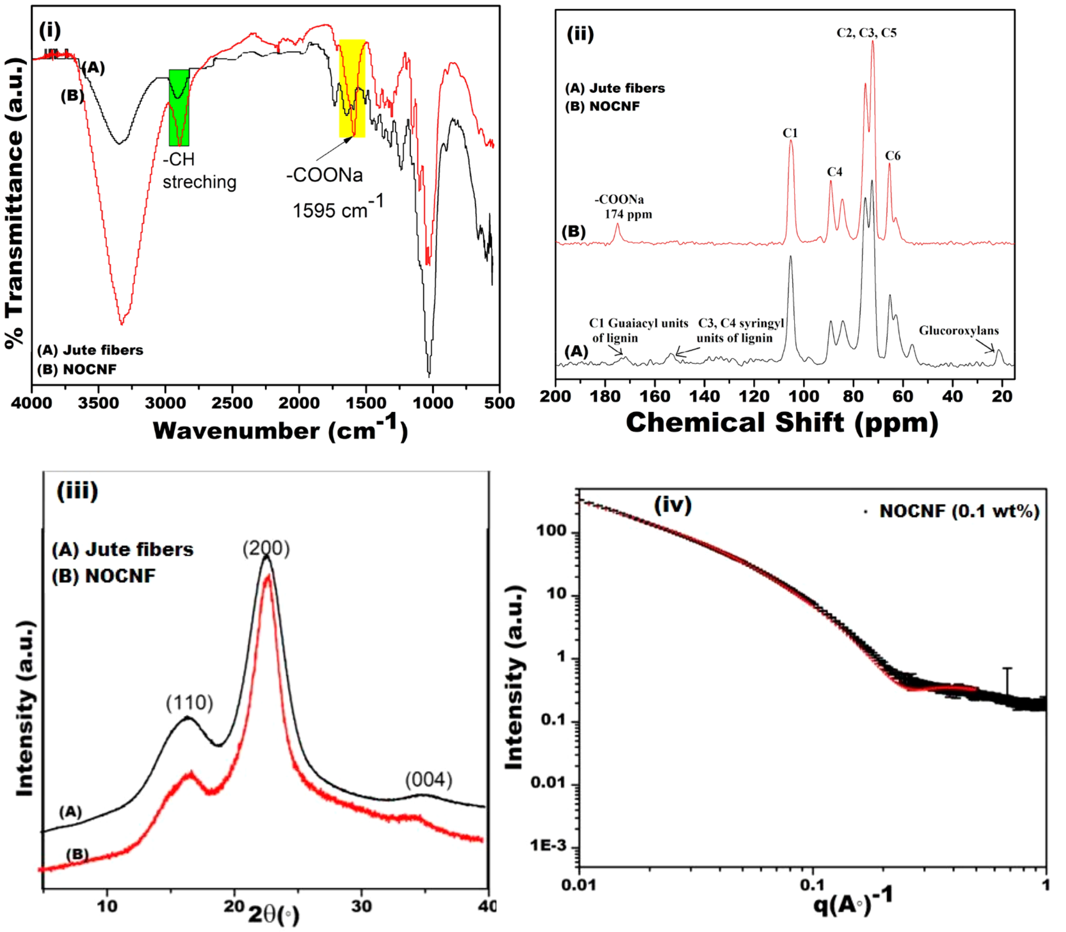

Figure 2. (i) FTIR spectra of jute fibers and NOCNF. (ii) ^{13}C CPMAS NMR spectra of jute fibers and NOCNF. (iii) WAXD patterns of jute fibers and NOCNF extracted using the nitro-oxidation method. (iv) SAXS profile of NOCNF (0.1 wt %) suspension and the fitting curve using the ribbon model.

STA-6000 Simultaneous thermal analyzer). The morphology of NOCNF was analyzed by transmission electron microscopy (TEM, FEI Tecnai G2 Spirit BioTWIN instrument), atomic force microscopy (AFM, Bruker Dimension ICON scanning probe microscope, Bruker Corporation), and solution small-angle X-ray scattering (SAXS) technique[37] (in the LiX beamline at the NSLS-II, Brookhaven National Laboratory). The surface area of freeze-dried NOCNF was measured by the Brunauer−Emmett−Teller (BET) analyzer (Quantachrome NOVAtouch LX2 analyzer).

Rheological measurements of NOCNF suspensions with different concentrations were carried out using a stress-controlled rheometer (TA Instruments AR-G2). In these measurements, a double-walled concentric cylinder holder was employed to evaluate the samples at concentrations of 0.05, 0.1, and 0.2 wt %, respectively, while a 40 mm parallel-plate holder was used to investigate the samples at concentrations of 0.4, 0.6, 0.8, and 1 wt %, respectively. The linear viscoelastic (LVE) region for NOCNF was obtained using the stress sweep measurements at a constant frequency of 1 Hz, where rheological responses of NOCNF samples were also determined by measuring the frequency sweeps within the LVE region. Finally, flow sweeps were carried out at the shear rate from 0.01 to 100 s^{-1}. All measurements were performed at 25 °C, and a solvent trap was used to prevent the solvent evaporation.

Preparation of Nanopaper. Nanopaper prepared from the NOCNF suspension was accomplished by vacuum filtration using a microfiltration assembly composed of a glass support Ultra-Ware glass funnel connected to a vacuum pump, where the funnel was fitted with a Durapore membrane filter paper having a diameter of 47 mm and an average pore size of 0.65 μm. A 200 mL portion of 0.2 wt % NOCNF suspension was slowly fed into the funnel using the glass rod to avoid the formation of air bubbles. The aggregation of the NOCNF layer was formed continuously on top of the membrane paper until a uniform wet sheet of NOCNF nanopaper was achieved. The wet nanopaper sheet was then removed from the membrane paper, and placed between two Kapton films and hot-pressed at 111 °C for 20 min. To avoid the wrinkling of the nanopaper edges, the resulting nanopaper was compressed under 1 kg of weight at room temperature for 16 h and then tested for mechanical properties.

Mechanical Evaluation of Nanopaper. To investigate the mechanical properties of NOCNF nanopaper samples, dynamic mechanical analysis (DMA Q800, TA Instruments, New Castle, DE) was employed to obtain the stress−strain measurements. Samples were first cut into dimensions of ~5 × 0.5 × 0.2 mm ($L \times W \times T$) and then mounted between two tension clamps with a preloading force of 0.03 N. Additional force was then applied on the sample at the rate of 3 N/min until the sample was fractured.

■ RESULTS AND DISCUSSION

Characterization of NOCNF. The nitro-oxidation approach was designed to treat raw biomass, especially nonwood biomass (e.g., those from underutilized sources), aiming to make the CNF extraction more facile, more sustainable, less chemical oriented, and less energy dependent. Based on our previous nitro-oxidation study,[29] the primary factor affecting the morphology and gelation properties of NOCNF was the amount and concentration of nitric acid used. Upon further investigation, we discovered that the increase in nitric acid concentration to 65−67% would lead to fiber degradation having an average fiber length (L) of 290 ± 40 and an average width (D) of 4−5 nm. However, the decrease in nitric acid concentration to 60% could result in high aspect ratio NOCNF having a significant portion of fiber length >1000 nm without changing the average width (in this study). It was thought that the fiber degradation by nitric acid in high concentration was due to the breakage of 1,4-glycosidic bonds in cellulose chains.

Typically, when CNF has a large aspect ratio and high surface charge, the suspension can result in a homogeneous gel. The NOCNF sample obtained in the current study clearly exhibited the gelation behavior as seen in two photographs of a 1 wt % NOCNF suspension (carboxylate content = 0.416 mmol/g, ζ-potential ∼ −70 mV) in the neutral condition (Figure S1 in the Supporting Information). In Figure S1i, when the sample vial was flipped to an upside down position, the gel was found to adhere strongly to the bottom of the vial. However, the gel became a liquidlike material (Figure S1ii) upon shaking for 30 s, which indicated the thixotropic behavior of this gel. The relations among structure, functionality, and rheological property of extracted NOCNF using 60% nitric acid concentration are discussed as follows.

Surface Functionality and Properties. The surface functionality characterization of NOCNF extracted from untreated jute fibers under the chosen nitro-oxidation conditions was first carried out by FTIR. The FTIR spectra of untreated jute fibers and NOCNF are presented in Figure 2i. In these spectra, the dominant 3328 cm^{-1} peak due to the —OH stretching and the weaker 2900 cm^{-1} peak due to the —CH symmetrical stretching (all from the cellulose component) were present in both untreated jute fibers and NOCNF samples. However, the peak at 1515 cm^{-1} due to the C=C aromatic symmetrical stretching in lignin and those at 1739, 1460, 1240, and 810 cm^{-1} due to xylan and glucomannan of hemicellulose were only present in untreated jute fibers. The absence or significant reduction of the peak intensity in FTIR associated with lignin and hemicellulose moieties in NOCNF indicated that the nitro-oxidation method is an effective approach to remove the lignin and hemicellulose components from jute fibers. Moreover, the appearance of a sharp 1595 cm^{-1} peak in NOCNF, along with the simultaneous decrease in the CH stretching at 2900 cm^{-1}, confirmed the oxidation of jute fibers at the C6 position of the anhydroglucose units. In other words, the nitro-oxidation provided an effective pathway to selectively oxidize the C6 hydroxyl groups in anhydroglucose units to carboxyl groups. The carboxylate content (0.416 mmol/g) in CNF was determined using the conductometric titration method.

The corresponding graph on conductivity measurement vs volume of NaOH is shown in Figure S2 (Supporting Information). Although the FTIR of NOCNF did not show any relevant peaks of aldehyde groups, the conductometric titration on NOCNF after further oxidation using sodium chlorite suggested that the aldehyde content was 0.095 mmol/g. The procedure of oxidation of NOCNF using sodium chlorite is also described in the Supporting Information. The corresponding graph on the conductivity values versus the volume of sodium hydroxide consumed is depicted in Figure S3. In our previous study, a higher concentration of nitric acid (65%) was used in the nitro-oxidation method, which probably resulted in NOCNF having only carboxylate content without any aldehyde functionality.

The solid state ^{13}C CPMAS NMR measurement was performed to investigate the effectiveness of the modified nitro-oxidation method (using a lower concentration nitric acid of 60%) in removing the lignin and hemicellulose components from jute fibers, while simultaneously oxidizing the cellulose components to produce NOCNF. The results are shown in Figure 2ii. In this figure, both NMR spectra of jute fibers and NOCNF showed characteristic cellulose peaks; i.e., the peaks in between 60 and 70 ppm represented the C6 carbon of primary hydroxyl group, the array of peaks between 70 and 80 ppm the C2, C3, and C5 carbons in the anhydroglucose units, the peaks between 80 and 95 ppm the C4 carbons, and the peaks between 100 and 110 ppm the C1 carbons in anhydroglucose units. However, the NMR spectra of jute fibers displayed distinct peaks at ∼21 and 56 ppm, which were relevant to glucuroxylans of the hemicellulose component. Furthermore, the small peaks at 153 and ∼172 ppm corresponded to C1 carbons of the guaiacyl unit and syringyl unit of the lignin component in jute fibers. The disappearance of lignin and hemicellulose peaks in the NMR spectra of NOCNF further confirmed the removal of both lignin and hemicellulose. The presence of the intense carboxyl peak in NOCNF at 174 ppm provided the evidence of oxidation of the cellulose component in jute fibers.

Other surface properties characterized included the ζ-potential, conductivity, and surface area of the freeze-dried sample. Figure S4i,ii (Supporting Information) illustrates the results from ζ-potential and conductivity measurements of NOCNF in suspension, which showed that the resulting NOCNF had an average surface charge around −70 mV and conductivity around 0.090 mS/cm. The surface area of the freeze-dried NOCNF sample was estimated by the BET measurement (Figure S4iii in the Supporting Information), which indicated the value of the resulting sample was 35 m^2/g.

Crystallinity and Crystal Structure. Based on the ^{13}C CPMAS NMR spectra (Figure 2ii), it appeared that there was no drastic change in the crystalline and noncrystalline peaks of C4 and C6 carbons between jute fibers and NOCNF. The crystallinity index (CI) of these samples could be estimated using the following equation for the peaks related to C4 carbons:[40]

$$\mathrm{CI} = \frac{\text{area between 87 and 93 ppm}}{\text{area between 80 and 93 ppm}} \times 100 \qquad (1)$$

where the area between the region 87−93 ppm is related to the crystalline phase, and the area between 80 and 93 ppm corresponds to the total contribution of the crystalline and noncrystalline phases. Using the above equation, the extracted NOCNF sample was found to possess a CI value of 65% (CI of untreated jute fibers was around 62%), which was further confirmed by WAXD to be discussed next. This indicated that the nitro-oxidation method with lower concentration nitric acid (60%) was quite efficient to preserve the crystallinity of NOCNF. In our previous study,[29] the observed NMR spectrum indicated the presence of large noncrystalline region in NOCNF, where the corresponding crystallinity was only about 35%.

WAXD measurements were carried out to confirm the crystallinity index as well as the crystal structure of NOCNF, where the results are illustrated in Figure 2iii. In this figure, it was seen that both WAXD patterns of jute fibers and NOCNF exhibited cellulose I structure having similar intensity distributions. Specifically, three similar diffraction peaks at 2θ angles of 16.5°, 22.7°, and 35.1° were seen in the two patterns,

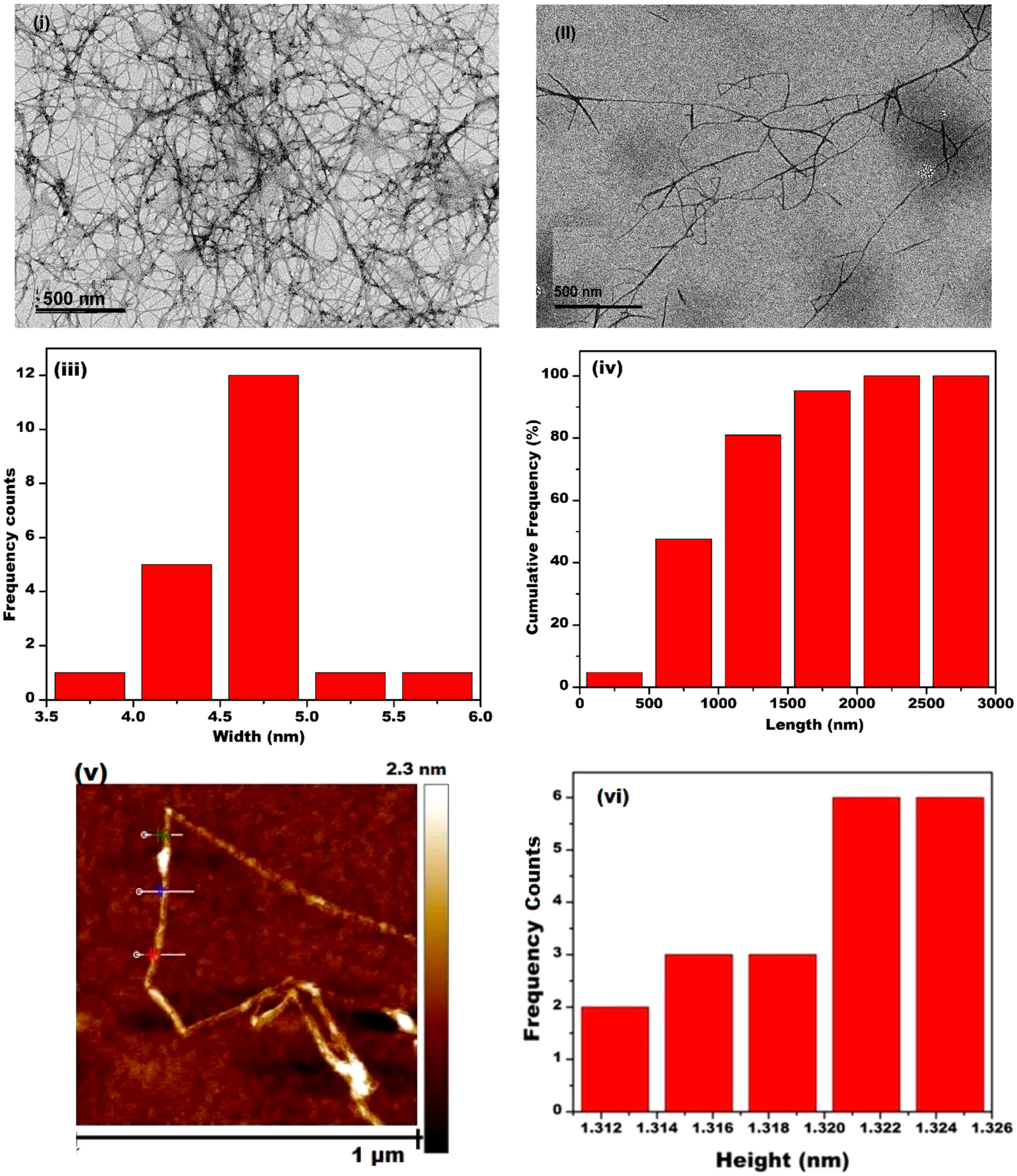

Figure 3. Morphology of extracted NOCNF showing (i) aggregated fibers in TEM and (ii) segregated fibers in TEM. (iii) Corresponding frequency counts of fiber width from TEM images. (iv) Frequency counts of fibers length from TEM images. (v) AFM image of NOCNF. (vi) Corresponding frequency counts of fiber thickness from AFM images.

corresponding to (110), (200), and (004) reflections, respectively.[41] This confirmed that the selected conditions in the nitro-oxidation reaction did not alter the crystal structure nor crystallinity in NOCNF when compared with those in untreated jute fibers. The crystallinity index (CI) calculated from the WAXD data using the Ruland method[40,41] for NOCNF was 69%, while that for jute fibers was 61%. These results are consistent with the CI values calculated from ^{13}C CPMAS NMR spectra. The slight increase of CI in NOCNF was expected, as untreated jute fibers contain only about 60% cellulose where the CI value in the initial cellulose phase should be much larger.

Morphology and Aspect Ratio. The morphology of NOCNF was characterized by TEM, where two typical images (one from aggregated fibers through the use of higher NOCNF concentration, and one from segregated fibers from the use of NOCNF lower concentration) and their length distributions are illustrated in Figure 3i,ii. These images showed that NOCNF extracted using nitric acid with 60% concentration possessed long filaments, entangled in a weblike fashion, where the lengths of the major portion of the fibers were significantly greater than 1000 nm (images were taken at the 500 nm scale, and even though, the length of some fibers could not be easily determined). The observation provided the strong evidence

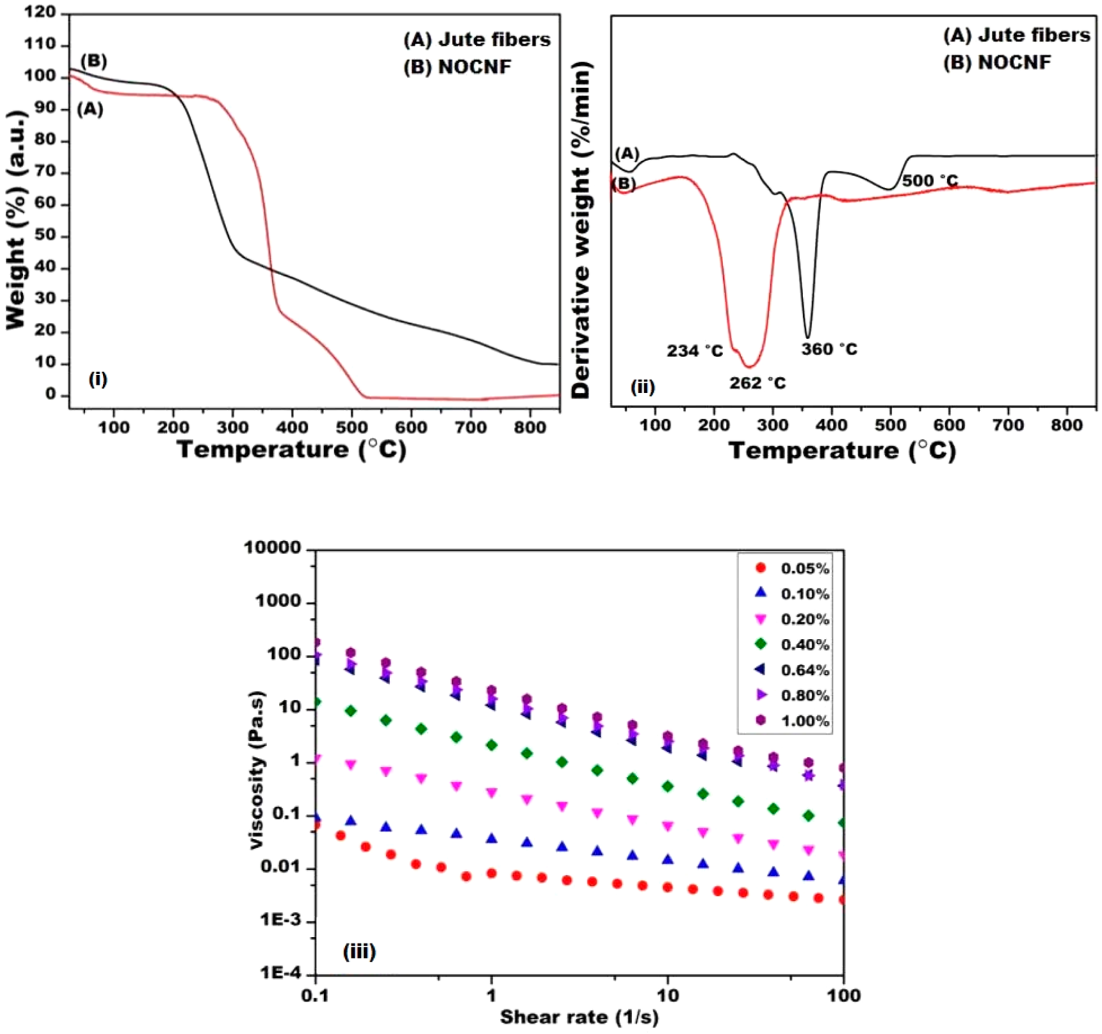

Figure 4. (i) TGA curves of jute fibers and NOCNF. (ii) DTG curves of jute fibers and NOCNF. (iii) Viscosity measurement of the NOCNF suspension at different NOCNF concentration (wt %) as a function of the shear rate.

that NOCNF extracted using the current nitro-oxidation reaction approach could result in high aspect ratio NOCNF from untreated jute fibers. The statistical width distribution of NOCNF (based on estimates from 30 fibers) is shown in Figure 3iii, where the average NOCNF width was found to be in 4.6 ± 0.95 nm. The statistical fiber length distribution of the same NOCNF system determined by a lower resolution TEM image is shown in Figure 3iv, which indicates that the range of the fiber length distribution falls in the range 200−2500 nm. The average length and width of NOCNF calculated for 30 fibers from these TEM images was 871 nm, and the corresponding *L*/*D* ratio was 189. Based on our previous work, the higher concentration (65%) of nitric acid led to NOCNF with an average length (*L*) of 290 ± 40 and an average width (*D*) of 4−5 nm.[29] The use of high concentration of nitric acid would yield a lower degree of polymerization in NOCNF, due to the degradation in cellulose chains through scission of the 1,4-glycosidic linkage. However, the use of lower concentration (less than 55%) of nitric acid could not result in full defibrillation of raw jute fibers, probably because of the insufficient dissolution of the lignin and hemicellulose components. This will be the subject of a future study regarding the effect of nitric acid concentration on the production of nanocelluloses from different biomass resources.

In the current study, with the combined effects of high aspect ratio, sufficient carboxylate content (0.416 mmol/g), and relatively high surface charge (−70 mV) of NOCNF, gelation was observed at a low concentration (0.2 wt %). Similar results have been observed with TEMPO-oxidized and carboxymethylated nanocelluloses, where the overlapping concentration also appeared to be at around 0.2 wt %.[42,43] Nechyporchuk et al.[42] reported the recent development in rheological studies on cellulose nanofibrils, and described the effects of concentration and ionic strength of CNF on rheological properties, such as gelation and shear-thinning thixotropic behavior. Li et al.[43] also investigated the rheological properties of cellulose nanocrystals (CNC) and demonstrated that CNC acted as an elastic gel at high concentration. The rheological results of the NOCNF system will be discussed in a later section.

AFM imaging of NOCNF was also carried out to determine the thickness profile of NOCNF. Figure 3v shows the AFM image of a typical NOCNF sample. In this image, it was seen that the long filament possessed multiple kinks as reported in a recent study.[44] It was reported that the kinks were probably resulted from the processing, which might also be the case here. In Figure 3v, the width of the fibers could not be estimated as it was in the same order of magnitude as the radius of the AFM tip. However, the thickness of the NOCNF was estimated by the vertical deviation (height) of the AFM tip. The frequency count for the fiber width at different position of the NOCNF from the AFM images is illustrated in Figure 3vi. The results indicated that the observed thicknesses of NOCNF were all in the range of 1.3 nm. This indicates that the cross-sectional shape of NOCNF is not round, but ribbonlike. This conclusion is also consistent with the results from solution SAXS characterization of NOCNF in suspension.

The SAXS intensity profile of the 0.1 wt % NOCNF suspension is shown in Figure 2iv. This profile was quite featureless, and could be fitted with a model, such as a cylindrical form factor[45] or a parallelepiped form factor.[46] In our previous study,[47] we demonstrated the use of a polydisperse ribbon model could successfully describe the SAXS data of TEMPO-oxidized cellulose nanofibers in suspension. The model is based on the assumption that the length of the fiber is infinitely long (e.g., above 200 nm or above the SAXS spatial solution), where two cross-section dimensions and their corresponding variances are the major factors affecting the scattered intensity. As the typical length of NOCNF was above 1000 nm (Figure 3), but the cross-sectional width and thickness are within the SAXS detection range, we argue that the polydisperse ribbon model is an appropriate model for the SAXS analysis. The fitting curve by the ribbon model (using the SasView software) is shown in Figure 2iv, which superimposed well with the measured intensity profile from the NOCNF (0.1 wt %) suspension. The results indicated that the ribbon's cross-section had an average width of 4.9 nm with variance of 0.12 nm, and an average thickness of 1.4 nm with variance of 0.12 nm. These results agreed well with the TEM and AFM results (i.e., the average width around 4.6 nm and thickness around 1.3 nm, respectively).

Thermal Properties. The thermal degradation profiles of jute fibers and NOCNF are illustrated in Figure 4. The profile for jute fibers (Figure 4iA) indicates that the sample underwent degradation in three major steps at 281, 376, and 520 °C, respectively. The initial onset temperature (T_{onset}) was at 281 °C (where about 8 wt % weight loss was seen), and the final offset temperature (T_{offset}) was at 520 °C. In contrast, the thermal degradation profile of NOCNF (Figure 4iB) exhibited only two degradation steps, whereby the initial onset temperature (T_{onset}) was at 199 °C (with 2.7 wt % weight loss), and the final offset temperature (T_{offset}) was at 306 °C (with 54.3 wt % weight loss). The shifting of the T_{onset} value to a lower temperature of NOCNF as compared to that of jute fibers indicated the lower thermal stability of NOCNF. This might be due to the presence of thermally unstable anhydroglucoronic moiety in NOCNF, which could be degraded at a lower temperature (199 °C) and release CO_2. The derivative thermogravimetry (DTG) analyses are illustrated in Figure 4iiA. The results indicated that jute fibers (Figure 4iiA) had three distinct decomposition peaks at (1) 500 °C due to the degradation of lignin, (2) 360 °C due to the degradation of cellulose, and (3) 292 °C due to the degradation of hemicellulose. However, the DTG curve of NOCNF displayed only two degradation peaks, which could be attributed to the degradation of anhydroglucoronic units and anhydroglucose units of cellulose chains at 234 and 262 °C, respectively. The lower degradation temperature of the cellulose component in NOCNF than in jute fibers also reflected the nanoscale dimensions of NOCNF.

Rheological and Gelation Properties of NOCNF. Figure 4iii illustrates the effect of shear rate on the viscosity of NOCNF suspensions at different concentrations. All suspensions displayed the shear-thinning behavior; i.e., the viscosity decreased with the increase of shear rate. We expect that this shear-thinning behavior is a consequence of the entanglement of NOCNF at low shear rate and the disentanglement of NOCNF at high shear rate, similar to the rheological properties of polymer solutions. In addition, the flow curves indicated that the viscosity of the suspension increased with NOCNF concentration, which was expected. Such a concentration effect was also consistent with the results from frequency sweep experiments as described below.

Oscillatory shear measurements were performed to study the linear viscoelastic properties of these suspensions. Figure 5i shows the storage and loss moduli G' and G'' as a function of oscillatory strain at a constant frequency of 1 Hz for NOCNF suspensions at different concentrations (0.05−1 wt %). It was seen that both G' and G'' values are independent of strain

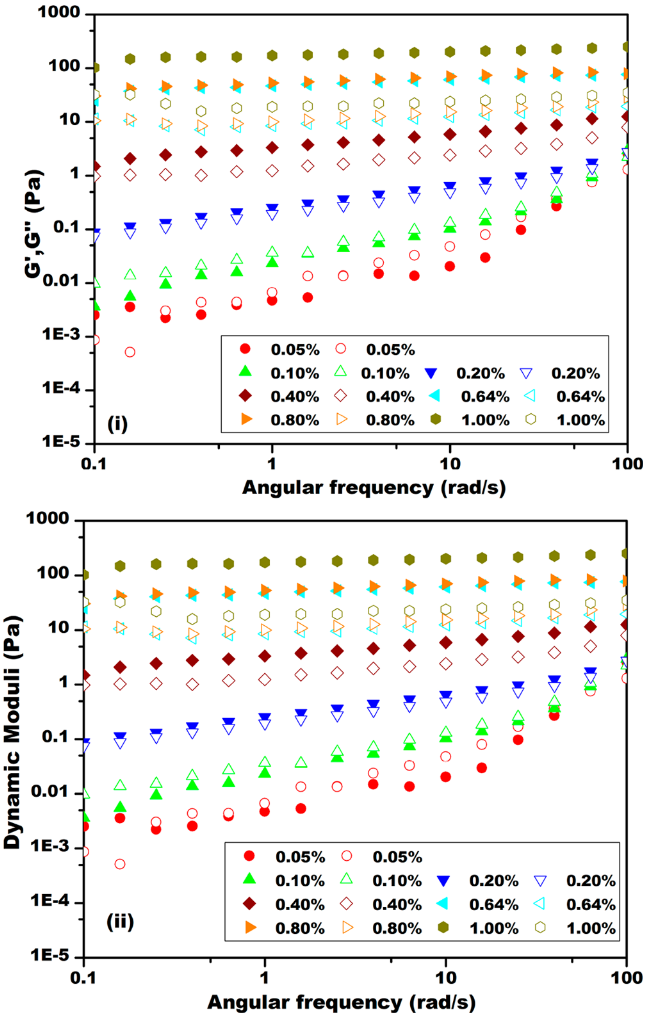

Figure 5. Storage and loss moduli as a function of (i) oscillatory strain at a constant frequency of 1 Hz, and (ii) oscillatory frequency at 0.1% strain for NOCNF suspensions at different concentrations (0.05−1 wt %). The closed symbol represents storage moduli (G'), while the open symbol represents loss moduli (G'').

below the strain value of 10% for all NOCNF suspensions. However, above 10% strain, G' decreased notably with the increase in strain, where the G'' also exhibited some interesting changes (for low concentration NOCNF suspensions, G'' also decreased slightly with strain; for high concentration NOCNF suspensions (≥0.64 wt %), G'' first increased and then decreased). The transition strains, where the G' and G'' changes were observed, seemed to be lower for higher concentration NOCNF suspensions. These results are consistent with the behavior of a gel structure resulted from the NOCNF network.

Figure 5ii shows G' and G'' as a function of oscillatory frequency at 0.1% strain for NOCNF suspensions at varying concentrations (0.05−1 wt %). At lower NOCNF concentrations (0.05−0.10 wt %), both G' and G'' were found to increase with increase in angular frequency, where G'' was greater than G'. This behavior could be characterized as that of a viscoelastic liquid. However, upon increasing the NOCNF concentration to 0.2 wt %, G' and G'' showed a weaker dependence on the frequency. Ultimately, at higher NOCNF concentrations, G' became greater than G'' over the range of measurable frequencies. This indicated a transition from a liquidlike behavior to a solidlike behavior due to the increase in NOCNF concentration. Upon further increase in NOCNF concentration (0.40−1.0 wt %), the magnitudes of G' and G'' became smaller and essentially independent of frequency.

Based on the rheological results in Figure 5, the critical gelation behavior appeared to occur at a concentration of about 0.2 wt %. This conclusion could be drawn clearly from Figure 5ii. In this figure, it was found that at 0.2 wt % NOCNF concentration, $G'(\omega) \approx G''(\omega)$ (ω is the angular frequency); i.e., both moduli exhibited roughly the same dependency on frequency. Winter and co-workers have identified this type of behavior as the critical point of polymer solution, where the liquid−gel transition occurs. To provide further insight into the nature of the fibrous NOCNF network at the gel point, G' and G'' values at 0.2 wt % concentration were analyzed according to the Winter−Chambon criterion,[48] and the results are shown in Figure 6i. This criterion predicts that both G' and G'' at the gel point should satisfy the relationship $G'(\omega) \approx G''(\omega) \propto \omega^n$, where n is a relaxation exponent with a value that falls in the range 0−1. The limit of $n \to 0$ indicates that the gel is elastic and stiff, whereas $n \to 1$ suggests that the gel is viscous and fragile.[49,50] In Figure 6i, the fitting of the frequency dependent NOCNF rheological data according to the Winter−Chambon model yielded $n \approx 0.5$, which has been observed in a wide variety of polymer and biopolymer networks at the gel point, including polyurethane,[51] chitosan,[52] and methacrylated alginate.[52,53] This value of $n \approx 0.5$ is usually attributed to the polymer network structure reaching percolation at the gel point. Thus, we believe that the critical concentration at 0.2 wt % NOCNF might also be associated with the percolation threshold of the nanofibers in suspension. That is, at low concentrations of NOCNF (<0.2 wt %), the dispersion of nanofibers only results in the fiber entanglement in small clusters/domains, where the system behaves as a free-flowing liquid. However, at higher concentrations NOCNF, the fiber entanglement takes place in the entire volume and formed a network structure that dominates the rheological properties of the system.

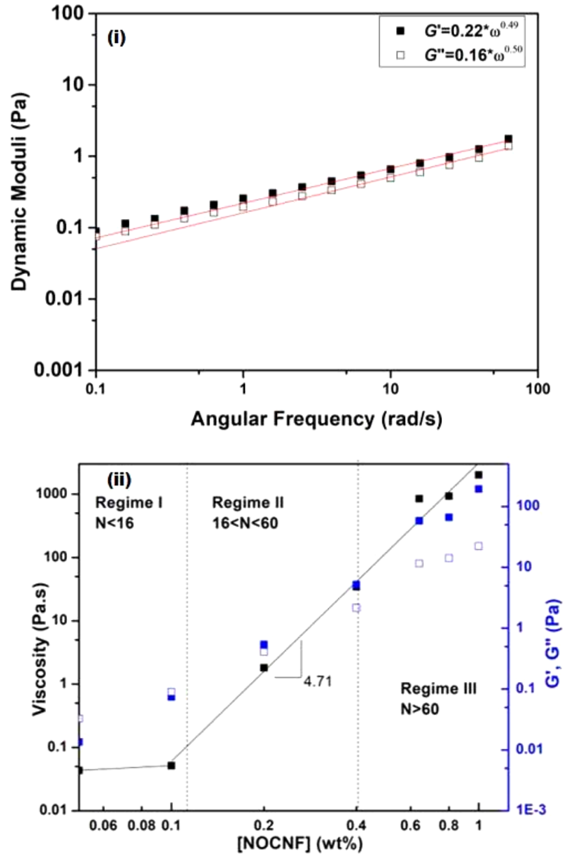

Figure 6. (i) G' and G'' as a function of frequency fitted by the Winter−Chambon model.[49] (ii) Steady shear viscosity (■) at shear rate of 0.01 s^{-1} and dynamic modulus (G', ■; G'', □) at 6.30 rad/s as a function of NOCNF concentration.

Relationship between Crowding Factor and Flow Properties. The flow properties of NOCNF suspensions at different concentrations (0.05, 0.1, and 0.2 wt %) were also determined by the crowding factor measured according to the Kerkes and Schell equation:[54]

$$N = \frac{2}{3}\varnothing\left(\frac{L}{D}\right)^2 \tag{2}$$

where N represents the crowding factor, L is the average length of fibers, D is the average diameter of fibers, and $\varnothing$ is the volume fraction of NOCNF. The relationships between NOCNF concentration, crowding factor, G' and G'' comparison, and behavior of the varying suspensions are summarized in Table 1. The concept of the crowding factor to describe the

Table 1. Relationships between NOCNF Concentration, Crowding Factor, G' and G' Comparison, and the Physical Behavior of the Suspension

concn of NOCNF	crowding factor (N)	G', G''	NOCNF behavior in suspension
0.05	7	$G' < G''$	fluidlike
0.1	15	$G' < G''$	fluidlike
0.2	30	$G' \approx G''$	gel-like
0.4	60	$G' > G''$	highly entangled “rigid” gel
0.64	89	$G' > G''$	highly entangled “rigid” gel
0.8	119	$G' > G''$	highly entangled “rigid” gel
1	149	$G' > G''$	highly entangled “rigid” gel

DOI: 10.1021/acsanm.8b00744
ACS Appl. Nano Mater. 2018, 1, 3969−3980

interactions and flocculation behavior in dispersion systems containing microscale fibers has been well documented.[55−57] In short, it can be mathematically derived that the fibers in a liquid suspension phase interact with each other in the spherical volume defined by the fiber diameter, known as the crowding factor (N). Recently, the concept of crowding factor has also been used to describe the rheological behavior of cellulose nanofibers (CNF) with surface changes.[58] For example, Geng et al. has examined the crowding factor in a series of CNF with different degree of oxidation of the fiber surface prepared by the TEMPO-mediated oxidation method. They reported that the N value is mainly dependent on the contact points of the nanofibers, which is a function of electrostatic interactions, aspect ratio (L/D), and concentration of nanofibers. The N value is also closely correlated with the viscosity and modulus data of the nanofiber dispersions. In brief, when $N < 16$ (Regime I), the CNF suspension should exhibit a fluid behavior; when $16 < N < 60$ (Regime II), the suspension should exhibit a soft gel behavior, and when $N > 60$ (Regime III), the system can be considered as a hard gel. This prediction agreed well with the results in Table 1. For example, in NOCNF suspensions with concentrations of 0.01, 0.05, and 0.1 wt %, the rheological results exhibited fluidlike behavior (Figure 4iii), where their corresponding N values were less than 16. At the NOCNF concentration around 0.2 wt % ($N = 30$), the system exhibited a liquid to gel transition, consistent with the prediction of the soft gel behavior. At higher NOCNF concentrations (>0.4 wt %), all N values were larger than 60; the systems exhibited a hard gel behavior.

The changes of viscosity at a low shear rate (i.e., 0.01 s^{-1}) and the dynamic moduli at a fixed frequency (6.3 rad/s) as a function of NOCNF concentration are illustrated in Figure 6ii. The low shear viscosity results revealed two distinct regimes, where the onset NOCNF concentration was around 0.1 wt %. This onset temperature was also referred to as the overlap concentration, which was consistent with the sol−gel transition point observed by the changes of the dynamic moduli as a function of NOCNF concentration (i.e., $G' = G''$ occurred at a value between 0.1 and 0.2 wt %). Based on the prediction of the crowding factor, 3 distinct regimes were also superimposed in Figure 6ii. It was found that, in Regime I ($N < 16$), $G'' > G'$ where the viscosity was the lowest, and it increased very slightly with concentration. This regime was clearly dominated by the fluid behavior. In Regime II ($16 < N < 60$), $G' \approx G''$, where the viscosity of the system increased rapidly with concentration. This regime contained the liquid−gel transition and exhibited the soft gel behavior. In Regime III ($N > 60$), $G' > G''$, where the viscosity of the system increased continuously. The slope of the viscosity changes versus NOCNF concentration in Regimes II and III was found to be 4.71, which is comparable to 4.82 as reported in polymer solutions by Matsuoka and Cowman.[60]

Mechanical Properties of NOCNF Nanopapers. Tensile properties of two nanopapers prepared from both high aspect ratio and low aspect ratio NOCNF are shown in Figure 7. The nanopaper prepared by the high aspect ratio NOCNF ($L = 871$ nm and $D = 4.8$ nm, $L/D = 189$) exhibited excellent mechanical properties with Young's modulus of 4.1 ± 0.2 GPa, tensile strength of 108 ± 2 MPa, and elongation at break ratio of 2.7 ± 0.2%. These values are significantly better than those of nanopaper samples prepared by the low aspect ratio NOCNF (e.g., $L = 290$ nm and $D = 4.5$ nm).[29] For example, the Young's modulus and tensile strength for the low aspect ratio NOCNF were about 1.1 ± 0.2 GPa and 1.3 MPa, respectively, with the elongation at break ratio about 1.2%. The most probable reason for such a low tensile strength is the decrease of fiber length using nitric acid at high concentrations (65−67%)[29] for preparation of NOCNF, which resulted in low aspect ratio. The comparison of tensile mechanical properties (Young's modulus, tensile strength, and elongation at break) of nanopapers prepared by CNF extracted using different methods (e.g., nitro-oxidation, TEMPO-oxidation, enzymatic treatment, homogenization, grinding) is illustrated in Table 2. It is apparent that the CNF extraction method, the biomass source, and the approach to prepare nanopapers all play a role to affect the final mechanical properties. It appeared that nanopapers extracted from wood by using either TEMPO-oxidation, grinding, or enzymatic treatment have shown the highest tensile strength between 122 and 350 MPa.[59−63] In fact, there are only very few works in the literature discussing the tensile properties of nanopapers prepared from nonwood sources such as spinifex-based CNF prepared by the homogenization process.[64] Our results indicated that nanopapers produced from NOCNF exhibited decent tensile properties, which might be greatly improved by better processing conditions.

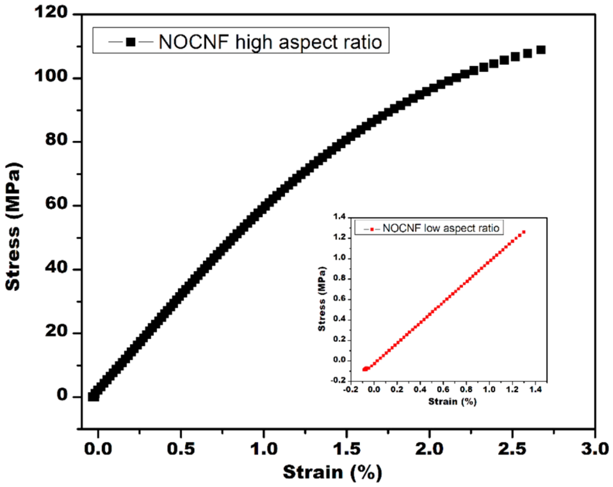

Figure 7. Tensile curve for nanopaper prepared from high aspect ratio NOCNF (with an average length of 871 nm and an average width of ~4.6 nm). Inset right: tensile curve of nanopaper prepared from low aspect ratio NOCNF (with an average length of 290 nm and an average width of ~4.5 nm).

■ CONCLUSIONS

This study showed that the reduction of the nitric acid concentration to the level of 60 wt % in the nitro-oxidation method could produce high aspect ratio cellulose nanofibers (NOCNF) with average length (L) = 871 nm, average width (D) of 4.6 nm, average thickness of 1.3 nm, carboxylate content of 0.416 mmol/g, and surface charge of −70 mV, from untreated jute fibers, where high crystallinity and strong gelation tendency could also be obtained (the crystallinity, measured by WAXD, of jute fibers was 61%, while that of NOCNF was 69%). The use of less concentrated nitric acid (60%) could lead to reduced consumption of acid, water, and chemicals (for neutralization and conversion of the effluent into a fertilizer), especially beneficial for scale up production. The rheological results indicated that the NOCNF suspensions

Table 2. Comparative Table on the Mechanical Properties of Nanopapers Prepared by NOCNF and CNF Using Other Methods

sample	Young's modulus (GPa)	tensile strain at break (%)	tensile stress (MPa)	preparation method	ref
NOCNF-jute (nitro-oxidation)	4.1 ± 0.2	2.7 ± 0.2	108 ± 2	vacuum filtration followed by hot pressing	this work
CNF-spinifex (homogenization)	3.2 ± 0.2	18.0 ± 0.2	84 ± 5	vacuum filtration, oven drying	64
TOCNF-wood pulp (TEMPO-oxidation)	6.6 ± 1.3	8.9 ± 0.9	237 ± 30	vacuum filtration, oven drying	61
CNF-eucalyptus pulp (enzymatic treatment)		16.3 ± 0.1	122 ± 1	vacuum filtration, oven drying	62
CNF-wood (mechanical grinding)	13		223	vacuum filtration	63
TOCNF-softwood (TEMPO-oxidation)	6.9 ± 1.4	7.6 ± 0.2	233 ± 44	suction filtration followed by oven drying	64
TOCNF-hardwood (TEMPO-oxidation)	6.2 ± 1.6	7.0 ± 2.4	222 ± 11	suction filtration followed by oven drying	64

exhibited shear-thinning and thixotropic behavior in a wide range of concentrations (0.01−1 wt %). This behavior was quite similar to the previously reported TEMPO-oxidized and carboxymethylated CNF.[42] The critical gelation concentration of NOCNF observed was between 0.1 and 0.2 wt %, based on the results of dynamic moduli. The characteristics of high aspect ratio carboxylated cellulose could lead to gelation, which greatly facilitates the production of water purification membranes and nanocomposite films. The rheological data beyond the gel point could be fitted by the Winter−Chambon model, where the behavior is consistent with the formation of a percolated network structure due to high aspect ratio of NOCNF. The concept of the crowding factor was also found to be able to predict the flow behavior of NOCNF suspensions in the entire concentration range investigated. Finally, the nanopaper produced using high aspect ratio carboxylated nanofibers suspension exhibited strong mechanical strength with tensile strength of 108 ± 2 MPa and Young's modulus of 4.1 ± 0.2 GPa, comparable to those of nanopapers produced by the other methods.

■ ASSOCIATED CONTENT

Ⓢ Supporting Information

The Supporting Information is available free of charge on the ACS Publications website at DOI: 10.1021/acsanm.8b00744.

> Experimental description of Fourier transform infrared spectrometry (FTIR), ^{13}C CPMAS NMR, wide-angle X-ray diffraction (WAXD), thermogravimetric analysis (TGA), transmission electron microscopy (TEM), atomic force microscopy (AFM), solution small-angle X-ray scattering (SAXS), surface area measurement using Brunauer−Emmett−Teller (BET) analysis, ζ-potential measurements, conductometric titration of NOCNF, and conductometric titration of NOCNF after further oxidation using sodium chlorite; picture of NOCNF suspension; conductivity graph of NOCNF after the nitro-oxidation treatment; conductivity graph of NOCNF after sodium chlorite ($NaClO_2$) oxidation; and graphs of ζ-potential, conductivity of NOCNF in suspension, and BET measurements of freeze-dried NOCNF sample (PDF)

■ AUTHOR INFORMATION

Corresponding Author

*Phone: +1 (631) 632-7793. E-mail: benjamin.hsiao@stonybrook.edu.

ORCID

Surita R. Bhatia: 0000-0002-5950-193X
Benjamin S. Hsiao: 0000-0002-3180-1826

Notes

The authors declare no competing financial interest.

■ ACKNOWLEDGMENTS

B.S.H. acknowledges the National Science Foundation (NSF DMR-1409507 and DMR-1808690), and S.R.B. acknowledges both NSF CBET-1335787 and ACS PRF 55729-ND9 for the financial support of this project. The authors would like to thank Dr. Chung-Chueh Chang and Mr. Ya-Chen Chuang (the ThINC facility at AERTC at Stony Brook University) for conducting the TEM analysis, and Dr. Martin Ziliox (NMR facility at Stony Brook University) for assisting the NMR analysis. The authors also are thankful to the SAXS (16-ID LiX) facility at National Synchrotron Light Source II (NSLS-II) in Brookhaven National Laboratory (BNL), where LiX has been supported by a DOE BER contract (DE-SC0012704) and an NIH-NIGMS grant (P41GM111244), and NSLS-II has been operated under a DOE BES contract (DE-SC0012704).

■ REFERENCES

(1) Wen, X.; Zheng, Y.; Wu, J.; Wang, L. N.; Yuan, Z.; Peng, J.; Meng, H. Immobilization of Collagen Peptide on Dialdehyde Bacterial Cellulose Nanofibers via Covalent Bonds for Tissue Engineering and Regeneration. *Int. J. Nanomed.* **2015**, *10*, 4623−37.

(2) Zhu, H.; Luo, W.; Ciesielski, P. N.; Fang, Z.; Zhu, J. Y.; Henriksson, G.; Himmel, M. E.; Hu, L. Wood-Derived Materials for Green Electronics, Biological Devices, and Energy Applications. *Chem. Rev.* **2016**, *116*, 9305−74.

(3) Sharma, R.; Alam, F.; Sharma, A. K.; Dutta, V.; Dhawan, S. K. ZnO Anchored Graphene Hydrophobic Nanocomposite-Based Bulk Heterojunction Solar Cells Showing Enhanced Short-Circuit Current. *J. Mater. Chem. C* **2014**, *2*, 8142−8151.

(4) Fang, Z.; Zhu, H.; Yuan, Y.; Ha, D.; Zhu, S.; Preston, C.; Chen, Q.; Li, Y.; Han, X.; Lee, S.; Chen, G.; Li, T.; Munday, J.; Huang, J.; Hu, L. Novel Nanostructured Paper with Ultrahigh Transparency and Ultrahigh Haze for Solar Cells. *Nano Lett.* **2014**, *14*, 765−73.

(5) Fukuzumi, H.; Fujisawa, S.; Saito, T.; Isogai, A. Selective Permeation of Hydrogen Gas using Cellulose Nanofibril Film. *Biomacromolecules* **2013**, *14*, 1705−9.

(6) Mahmoud, K. A.; Mena, J. A.; Male, K. B.; Hrapovic, S.; Kamen, A.; Luong, J. H. Effect of Surface Charge on the Cellular Uptake and Cytotoxicity of Fluorescent Labeled Cellulose Nanocrystals. *ACS Appl. Mater. Interfaces* **2010**, *2*, 2924−32.

(7) Sharma, P. R.; Kamble, S.; Sarkar, D.; Anand, A.; Varma, A. J. Shape and Size Engineered Cellulosic Nanomaterials as Broad

Spectrum Anti-microbial Compounds. *Int. J. Biol. Macromol.* **2016**, *87*, 460−5.

(8) Shah, K. J.; Imae, T. Selective Gas Capture Ability of Gas-Adsorbent-Incorporated Cellulose Nanofiber Films. *Biomacromolecules* **2016**, *17*, 1653−61.

(9) Suopajärvi, T.; Liimatainen, H.; Hormi, O.; Niinimäki, J. Coagulation−Flocculation Treatment of Municipal Wastewater Based on Anionized Nanocelluloses. *Chem. Eng. J.* **2013**, *231*, 59−67.

(10) Ma, H.; Hsiao, B. S.; Chu, B. Ultrafine Cellulose Nanofibers as Efficient Adsorbents for Removal of UO22+in Water. *ACS Macro Lett.* **2012**, *1*, 213−216.

(11) Ghosh, A. K.; Bandyopadhyay, P. A Simple Strategy for Charge Selective Biopolymer Sensing. *Chem. Commun. (Cambridge, U. K.)* **2011**, *47*, 8937−9.

(12) Sharma, P. R.; Varma, A. J. Functional Nanoparticles obtained from Cellulose: Engineering the Shape and Size of 6-Carboxycellulose. *Chem. Commun. (Cambridge, U. K.)* **2013**, *49*, 8818−20.

(13) Ji, S.; Hyun, B. G.; Kim, K.; Lee, S. Y.; Kim, S.-H.; Kim, J.-Y.; Song, M. H.; Park, J.-U. Photo-Patternable and Transparent Films using Cellulose Nanofibers for Stretchable Origami Electronics. *NPG Asia Mater.* **2016**, *8*, e299.

(14) Kang, W.; Yan, C.; Foo, C. Y.; Lee, P. S. Foldable Electrochromics Enabled by Nanopaper Transfer Method. *Adv. Funct. Mater.* **2015**, *25*, 4203−4210.

(15) Ji, S.; Jang, J.; Cho, E.; Kim, S.-H.; Kang, E.-S.; Kim, J.; Kim, H.-K.; Kong, H.; Kim, S.-K.; Kim, J.-Y.; Park, J.-U. High Dielectric Performances of Flexible and Transparent Cellulose Hybrid Films Controlled by Multidimensional Metal Nanostructures. *Adv. Mater.* **2017**, *29*, 1700538.

(16) Lu, Y.; Ye, G.; She, X.; Wang, S.; Yang, D.; Yin, Y. Sustainable Route for Molecularly Thin Cellulose Nanoribbons and Derived Nitrogen-Doped Carbon Electrocatalysts. *ACS Sustainable Chem. Eng.* **2017**, *5*, 8729−8737.

(17) Kaushik, M.; Basu, K.; Benoit, C.; Cirtiu, C. M.; Vali, H.; Moores, A. Cellulose Nanocrystals as Chiral Inducers: Enantioselective Catalysis and Transmission Electron Microscopy 3D Characterization. *J. Am. Chem. Soc.* **2015**, *137*, 6124−7.

(18) Xu, X.; Liu, F.; Jiang, L.; Zhu, J. Y.; Haagenson, D.; Wiesenborn, D. P. Cellulose Nanocrystals vs. Cellulose Nanofibrils: A Comparative Study on their Microstructures and Effects as Polymer Reinforcing Agents. *ACS Appl. Mater. Interfaces* **2013**, *5*, 2999−3009.

(19) Reid, M. S.; Villalobos, M.; Cranston, E. D. Benchmarking Cellulose Nanocrystals: From the Laboratory to Industrial Production. *Langmuir* **2017**, *33*, 1583−1598.

(20) Lin, J.; Yu, L.; Tian, F.; Zhao, N.; Li, X.; Bian, F.; Wang, J. Cellulose Nanofibrils Aerogels Generated from Jute Fibers. *Carbohydr. Polym.* **2014**, *109*, 35−43.

(21) Isogai, A.; Saito, T.; Fukuzumi, H. TEMPO-Oxidized Cellulose Nanofibers. *Nanoscale* **2011**, *3*, 71−85.

(22) Siró, I.; Plackett, D. Microfibrillated Cellulose and New Nanocomposite Materials: a Review. *Cellulose* **2010**, *17*, 459−494.

(23) Sharma, P. R.; Varma, A. J. Functionalized Celluloses and their Nanoparticles: Morphology, Thermal Properties, and Solubility Studies. *Carbohydr. Polym.* **2014**, *104*, 135−42.

(24) Sharma, P. R.; Rajamohanan, P. R.; Varma, A. J. Supramolecular Transitions in Native Cellulose-I during Progressive Oxidation Reaction leading to Quasi-Spherical Nanoparticles of 6-Carboxycellulose. *Carbohydr. Polym.* **2014**, *113*, 615−23.

(25) Sadeghifar, H.; Filpponen, I.; Clarke, S. P.; Brougham, D. F.; Argyropoulos, D. S. Production of Cellulose Nanocrystals using Hydrobromic Acid and Click Reactions on their Surface. *J. Mater. Sci.* **2011**, *46*, 7344−7355.

(26) Camarero Espinosa, S.; Kuhnt, T.; Foster, E. J.; Weder, C. Isolation of Thermally Stable Cellulose Nanocrystals by Phosphoric Acid Hydrolysis. *Biomacromolecules* **2013**, *14*, 1223−30.

(27) Yu, H.-Y.; Zhang, D.-Z.; Lu, F.-F.; Yao, J. New Approach for Single-Step Extraction of Carboxylated Cellulose Nanocrystals for Their Use As Adsorbents and Flocculants. *ACS Sustainable Chem. Eng.* **2016**, *4*, 2632−2643.

(28) Saito, T.; Okita, Y.; Nge, T. T.; Sugiyama, J.; Isogai, A. TEMPO-mediated Oxidation of Native Cellulose: Microscopic Analysis of Fibrous Fractions in the Oxidized Products. *Carbohydr. Polym.* **2006**, *65*, 435−440.

(29) Sharma, P. R.; Joshi, R.; Sharma, S. K.; Hsiao, B. S. A Simple Approach to Prepare Carboxycellulose Nanofibers from Untreated Biomass. *Biomacromolecules* **2017**, *18*, 2333−2342.

(30) Chinga-Carrasco, G.; Syverud, K. Pretreatment-Dependent Surface Chemistry of Wood Nanocellulose for pH-sensitive Hydrogels. *J. Biomater. Appl.* **2014**, *29*, 423−32.

(31) Liimatainen, H.; Suopajarvi, T.; Sirvio, J.; Hormi, O.; Niinimaki, J. Fabrication of Cationic Cellulosic Nanofibrils through Aqueous Quaternization Pretreatment and their use in Colloid Aggregation. *Carbohydr. Polym.* **2014**, *103*, 187−92.

(32) Cao, X.; Ding, B.; Yu, J.; Al-Deyab, S. S. Cellulose Nanowhiskers Extracted from TEMPO-Oxidized Jute Fibers. *Carbohydr. Polym.* **2012**, *90*, 1075−80.

(33) Yu, H.; Qin, Z.; Liang, B.; Liu, N.; Zhou, Z.; Chen, L. Facile Extraction of Thermally Stable Cellulose Nanocrystals with a High Yield of 93% through Hydrochloric Acid Hydrolysis under Hydrothermal Conditions. *J. Mater. Chem. A* **2013**, *1*, 3938.

(34) Sharma, P. R.; Chattopadhyay, A.; Sharma, S. K.; Hsiao, B. S. Efficient Removal of UO22+ from Water Using Carboxycellulose Nanofibers Prepared by the Nitro-Oxidation Method. *Ind. Eng. Chem. Res.* **2017**, *56*, 13885−13893.

(35) Dimmel, D. R.; Karim, M. R.; Savidakis, M. C.; Bozell, J. J. Pulping Catalysts From Lignin (5). Nitrogen Dioxide Oxidation Of Lignin Models To Benzoquinones. *J. Wood Chem. Technol.* **1996**, *16*, 169−189.

(36) Jacobsen, S. E.; Wyman, C. E. Cellulose and Hemicellulose Hydrolysis Models for Application to Current and Novel Pretreatment Processes. *Appl. Biochem. Biotechnol.* **2000**, *84−86*, 81−96.

(37) Ma, H.; Burger, C.; Hsiao, B. S.; Chu, B. Nanofibrous Microfiltration Membrane based on Cellulose Nanowhiskers. *Biomacromolecules* **2012**, *13*, 180−6.

(38) Ma, H.; Burger, C.; Hsiao, B. S.; Chu, B. Ultra-Fine Cellulose Nanofibers: New Nano-Scale Materials for Water Purification. *J. Mater. Chem.* **2011**, *21*, 7507.

(39) Olivera, S.; Muralidhara, H. B.; Venkatesh, K.; Guna, V. K.; Gopalakrishna, K.; Kumar, K. Y. Potential Applications of Cellulose and Chitosan Nanoparticles/Composites in Wastewater Treatment: A Review. *Carbohydr. Polym.* **2016**, *153*, 600−618.

(40) Knaus, S.; Bauer-Heim, B. Synthesis and Properties of Anionic Cellulose Ethers: Influence of Functional Groups and Molecular Weight on Flowability of Concrete. *Carbohydr. Polym.* **2003**, *53*, 383−394.

(41) Chidambareswaran, P. K.; Sreenivasan, S.; Patil, N. B. Quantitative-Analysis of Crystalline Phases in Chemically Treated Cotton Fibers. *Text. Res. J.* **1987**, *57*, 219−222.

(42) Nechyporchuk, O.; Belgacem, M. N.; Pignon, F. Current Progress in Rheology of Cellulose Nanofibril Suspensions. *Biomacromolecules* **2016**, *17*, 2311−20.

(43) Li, M.-C.; Wu, Q.; Song, K.; Lee, S.; Qing, Y.; Wu, Y. Cellulose Nanoparticles: Structure−Morphology−Rheology Relationships. *ACS Sustainable Chem. Eng.* **2015**, *3*, 821−832.

(44) Usov, I.; Nystrom, G.; Adamcik, J.; Handschin, S.; Schutz, C.; Fall, A.; Bergstrom, L.; Mezzenga, R. Understanding Nanocellulose Chirality and Structure-Properties Relationship at the Single Fibril Level. *Nat. Commun.* **2015**, *6*, 7564.

(45) Uhlig, M.; Fall, A.; Wellert, S.; Lehmann, M.; Prevost, S.; Wagberg, L.; von Klitzing, R.; Nystrom, G. Two-Dimensional Aggregation and Semidilute Ordering in Cellulose Nanocrystals. *Langmuir* **2016**, *32*, 442−50.

(46) Cherhal, F.; Cousin, F.; Capron, I. Influence of Charge Density and Ionic Strength on the Aggregation Process of Cellulose Nanocrystals in Aqueous Suspension, as Revealed by Small-Angle Neutron Scattering. *Langmuir* **2015**, *31*, 5596−602.

(47) Su, Y.; Burger, C.; Hsiao, B. S.; Chu, B. Characterization of TEMPO-Oxidized Cellulose Nanofibers in Aqueous Suspension by Small-Angle X-Ray Scattering. *J. Appl. Crystallogr.* **2014**, *47*, 788−798.

(48) Winter, H. H.; Chambon, F. Analysis of Linear Viscoelasticity of a Crosslinking Polymer at the Gel Point. *J. Rheol. (Melville, NY, U. S.)* **1986**, *30*, 367−382.

(49) Pan, Y.; Li, L. Percolation and Gel-like Behavior of Multiwalled Carbon Nanotube/Polypropylene Composites Influenced by Nanotube Aspect Ratio. *Polymer* **2013**, *54*, 1218−1226.

(50) Sharma, N.; Kasi, R. M. Dynamic Viscoelasticity and Concentration Dependence of Micelle−Gel Transition of Styrene and N-tert-Butylacrylamide Diblock Copolymer Solutions. *Langmuir* **2010**, *26*, 7418−7424.

(51) Winter, H. H. Evolution of rheology during chemical gelation. In *Permanent and Transient Networks*; Steinkopff: Darmstadt, 1987; pp 104−110.

(52) Chenite, A.; Chaput, C.; Wang, D.; Combes, C.; Buschmann, M. D.; Hoemann, C. D.; Leroux, J. C.; Atkinson, B. L.; Binette, F.; Selmani, A. Novel Injectable Neutral Solutions of chitosan form Biodegradable Gels InSitu. *Biomaterials* **2000**, *21*, 2155−2161.

(53) Bonino, C. A.; Samorezov, J. E.; Jeon, O.; Alsberg, E.; Khan, S. A. Real-time InSitu Rheology of Alginate Hydrogel Photocrosslinking. *Soft Matter* **2011**, *7*, 11510−11517.

(54) Kerekes, R.; Schell, C. Regimes by a Crowding Factor. *J. Pulp Pap. Sci.* **1992**, *18*, J32−J38.

(55) Mason, S. The flocculation of Pulp Suspensions and the Formation of Paper. *Tappi* **1950**, *33*, 440−444.

(56) Schmid, C. F. *Simulations of Flocculation in Flowing Fiber Suspensions*; University of Wisconsin—Madison, 1999.

(57) Schmid, C. F.; Switzer, L. H.; Klingenberg, D. J. Simulations of Fiber Flocculation: Effects of Fiber Properties and Interfiber Friction. *J. Rheol. (Melville, NY, U. S.)* **2000**, *44*, 781−809.

(58) Geng, L.; Mittal, N.; Zhan, C.; Ansari, F.; Sharma, P. R.; Peng, X.; Hsiao, B. S.; Söderberg, L. D. Understanding the Mechanistic Behavior of Highly Charged Cellulose Nanofibers in Aqueous Systems. *Macromolecules* **2018**, *51*, 1498−1506.

(59) Sun, X.; Wu, Q.; Ren, S.; Lei, T. Comparison of Highly Transparent All-Cellulose Nanopaper Prepared using Sulfuric Acid and TEMPO-mediated Oxidation Methods. *Cellulose* **2015**, *22*, 1123−1133.

(60) Nie, S.; Zhang, K.; Lin, X.; Zhang, C.; Yan, D.; Liang, H.; Wang, S. Enzymatic Pretreatment for the Improvement of Dispersion and Film Properties of Cellulose Nanofibrils. *Carbohydr. Polym.* **2018**, *181*, 1136−1142.

(61) Nogi, M.; Iwamoto, S.; Nakagaito, A. N.; Yano, H. Optically Transparent Nanofiber Paper. *Adv. Mater.* **2009**, *21*, 1595−1598.

(62) Fukuzumi, H.; Saito, T.; Iwata, T.; Kumamoto, Y.; Isogai, A. Transparent and High Gas Barrier Films of Cellulose Nanofibers Prepared by TEMPO-Mediated Oxidation. *Biomacromolecules* **2009**, *10*, 162−165.

(63) Zhu, M.; Wang, Y.; Zhu, S.; Xu, L.; Jia, C.; Dai, J.; Song, J.; Yao, Y.; Wang, Y.; Li, Y.; Henderson, D.; Luo, W.; Li, H.; Minus, M. L.; Li, T.; Hu, L. Anisotropic, Transparent Films with Aligned Cellulose Nanofibers. *Adv. Mater.* **2017**, *29*, 1606284.

(64) Amiralian, N.; Annamalai, P. K.; Memmott, P.; Taran, E.; Schmidt, S.; Martin, D. J. Easily Deconstructed, High Aspect Ratio Cellulose Nanofibres from Triodia pungens; an Abundant Grass of Australia's Arid Zone. *RSC Adv.* **2015**, *5*, 32124−32132.